Monthly Notices
of the
ROYAL ASTRONOMICAL SOCIETY

MNRAS **484,** 1057–1071 (2019)
Advance Access publication 2018 December 29

doi:10.1093/mnras/sty3515

The expansion of debris flow shed from the primary of 65803 Didymos

Y. Yu [1]★ P. Michel,[2] M. Hirabayashi [3] and D. C. Richardson[4]

[1]*School of Aeronautic Science and Engineering, Beihang University, Beijing 100191, China*
[2]*University of Nice Sophia Antipolis, CNRS, Observatoire de la Côte d'Azur, B.P. 4229, F-06304 Nice Cedex 4, France*
[3]*Department of Aerospace Engineering, Auburn University, 211 Davis Hall, AL 36849, USA*
[4]*Department of Astronomy, University of Maryland, College Park, MD 20742, USA*

Accepted 2018 December 17. Received 2018 December 15; in original form 2018 August 27

ABSTRACT

This paper investigates the plausible mass shedding from the surface of Didymos A, the primary of Near-Earth binary asteroid 65803 Didymos, and the subsequent orbital evolution of the shedding debris. Shedding conditions are derived semi-analytically. The unstable surface area on Didymos A is determined by combining the analyses and numeric results of SSDEM simulations. We show the observation-based model gives a highly unstable surface for Didymos A. In particular, most of the equatorial ridge is unattachable for cohesionless regolith, and an active region emerges along the ridge, in which extensive avalanches that cause surface mass shedding seem likely to happen. We track the ballistic motion of shedding debris from the unstable area. Month-long simulations show the diverse evolutions of sample particles with different sizes, due to the varying magnitude of solar radiation pressure. Statistics on the dynamical fates of shedding debris give clues on the current development of this binary system. Depending on the observation-based reference model, we find a vast majority of the shedding mass is finally transferred to Didymos B and thus leads to a cumulative growth. The cumulated mass may cause a spiralling-in motion of Didymos B, and the spiralling-in speed depends on the frequency and magnitude of mass shedding. A topography dependence of the mass shedding/transfer is also noticed that the cumulated mass mostly originates from highly elevated regions of the ridge areas. Long term it suggests that the shedding processes prefer to erode the bulges first and force the equatorial ridge to evolve into good roundness.

Key words: planets and satellites: dynamical evolution and stability – planets and satellites: formation – planets and satellites: individual: 65803 Didymos – planets and satellites: surfaces.

1 INTRODUCTION

The Near-Earth binary asteroid 65803 Didymos (1996 GT) is now targeted by the ESA–NASA joint space mission project AIDA (abbreviated for 'Asteroid Impact & Deflection Assessment'). The mission proposes to perform an asteroid deflection demonstration using a half-ton projectile that will impact on the surface of Didymos B, the smaller one of the binary system (Cheng et al. 2016). Through the impact experiment and direct measurements of the impact outcomes, the mission provides a unique opportunity to characterize the components of a binary asteroid system from a dynamical point of view, i.e. the large-scale cratering process, the physical properties of the ejecta plume, etc. (Michel et al. 2017). These are crucial information for understanding the surface, subsurface, and internal structures of the binary components, and will help reveal the roles of the key physical properties in the binary's dynamic behaviour.

As a target whose dynamics have already been characterized from ground-based observations (Pravec et al. 2006; Scheirich & Pravec 2009; Benner et al. 2010a), Didymos actually represents a special class of binary asteroids, whose primaries are below 10 km in diameter, with largely spherical shapes and high spin rates close to the critical values that cause rotational disruption (Ostro et al. 2006; Brozović et al. 2011; Pravec et al. 2012).

A plausible origin of binary asteroids like Didymos is provided by the YORP theory, which describes a 'rubble pile' progenitor being spun-up by the thermal recoil torque that eventually causes rotational breakup from the equator (Bottke et al. 2002; Ćuk 2007). The material transferred into the orbit provides the initial seeds of the secondary, which grows up by gradually accreting the mass lost from the progenitor's equator (Scheeres 2007; Pravec et al. 2010; Walsh & Jacobson 2015). Walsh et al. (2008, 2012) applied the hard-sphere discrete element method to mimic cohesionless gravitational aggregates that experience the YORP acceleration, showing that the equatorial ridge of the primary and the small satellite of binary asteroid 1999 KW4 may be both the products

★ E-mail: yuyang.thu@gmail.com

of continuously increasing angular momentum. This theory agrees with several observational results, including the non-gravitational acceleration/deceleration of some asteroids below 10 km and the accompanying progressive tilt of spin vectors (Kaasalainen et al. 2007; Taylor et al. 2007), and the unusually large number of small asteroids that have equatorial ridges (also known as 'top-shaped asteroids'; see Ostro et al. 2006; Brozović et al. 2011; Busch et al. 2011; Nolan et al. 2013; Benner et al. 2015). Special attention has also been paid to the structural stability of a rubble-pile progenitor when it evolves to near the critical spin limit (Hirabayashi et al. 2015, 2016; Scheeres 2015; Zhang et al. 2017). The results of these studies indicate that the failure modes and yield conditions of such small bodies depend strongly on both the internal configuration and material properties.

These studies have, from a macroscopic view, improved our understanding of the geological evolution of small asteroids driven by the YORP effect. In contrast to the discussion on these macro processes, our knowledge of the local regolith evolution during a YORP spin-up is still limited, which is partly because most data bases from remote observations are insufficient to support detailed topographic models. However, as we already know, the microscopic heterogeneity and discrete nature of the regolith layer play an important role in local surface failures (Zhang et al. 2017), which offers a key to understanding the evolution status of a specific binary system: on one hand, since the YORP spin-up is very slow (a theoretical estimate of the YORP time-scale for kilometer-sized Near-Earth Asteroid is 10^4 to 10^6 yr according to Rubincam 2000), small-scale avalanches and mass shedding may occur intermittently in various local places even before the critical spin limit that corresponds to a catastrophic global distortion is reached (Walsh et al. 2008). Each of these regional failures will contribute to determining the configuration of the binary components in subsequent phases. A typical example is provided by Harris et al. (2009), who investigated the shapes of several nearly critically spinning asteroids and found the loose regolith material undergoing a migration on the primary's equator can deliver some angular momentum to the moon's orbit. On the other hand, Statler (2009) shows the magnitude of YORP torque is inherently sensitive to small-scale topography, thus the spin-up effect may be strongly influenced by regular modifications in the surface topography caused by the 'space weathering' processes, such as the regolith redistributions resulting from planetary encounters, micrometeorite bombardments, and thermal fatigue, etc. (Clark et al. 2002). The coupling between the asteroid's rotation and shape puts a new uncertainty in determining the current status of the binary's evolution (Cotto-Figueroa et al. 2015), which makes it necessary to account for the local topographic effect when considering the regolith transport on the surface of and between the binary components.

Based on this understanding, we investigate the unstable regions on the surface of the primary of Didymos (called hereafter Didymos A), where the weathered material is capable of escaping with only a small kick-start in energy. The influence of the heterogenous terrain is considered by introducing a three-dimensional shape model represented in spherical harmonics. We derive the shedding-off conditions for loose debris flow sliding on the surface of the primary, and screen out those at risk of losing mass within a decametre-scale landslide in length. The subsequent motion of the lofted debris flow is then traced by using a previously developed numerical model that contains the major perturbation forms (Yu et al. 2017). We demonstrate the dynamics of the shedding debris flow as a function of the average particle size, and explore the topography dependence of particles that have different fates. By comparing the dynamical behaviours of debris flow under different set-ups, we can unveil essential information contained in the observational data, which could be beneficial to address questions like how the growth of the moonlet depends on the configuration of the binary, and for AIDA mission, what debris environment will a precursor spacecraft be exposed to.

The remainder of the paper is organized as follows. Section 2 derives the shedding-off conditions, which apply to Didymos A, and maps out the high-risk regions. Section 3 simulates the orbital evolution of the debris flow shed from these regions, and gives a statistical analysis of the shedding mass, showing how their dynamical fates depend on the particle size and on the topography of the launching position. Section 4 provides a brief review of the results and draws conclusions.

2 OBSERVATIONAL CONSTRAINTS ON THE SHEDDING MECHANICS

2.1 Reference models for asteroid 65803 Didymos

The Apollo-class Near-Earth Asteroid Didymos was detected in 1996 and its satellite was found by light-curve measurements in 2003 (Pravec et al. 2006). Combined radar and photometric observations of the past several years give some immediate information of the binary system, including the period of the mutual orbit, the mean separation of the two components, the rotation period of the primary, and the size ratio of the secondary to the primary (Pravec et al. 2006; Benner et al. 2010a; see Table 1). Other physical parameters were then derived from the measured properties. A shape model of the primary was also determined by the combined observations (Benner et al. 2010b), which has a resolution finer than 50 m and gives the current reference value of the bulk density that is applied later in the analyses of the dynamical properties (Dell'Elce et al. 2017; Yu et al. 2017; Zhang et al. 2017). But limited by the substantial uncertainty in the assessment of the volume, the reasonable bulk density lies within a wide range, i.e. 2.146 $\mathrm{g\,cc^{-1}}$ $\pm$30 per cent, which increases the difficulty in diagnosing the internal structural change of the primary at the current stage. An updated shape model will help to narrow down the range of bulk density, which is, however, still insufficient to show any small-scale terrains on the primary's surface. A shape model with resolution up to decimetre scale will be only available after the primary is closely visited by a spacecraft.

Based on the parameters adopted in the current reference model (Table 1), the rotation period of Didymos A, 2.26 h, is very close to the critical spin limit for homogenous spherical bodies (Harris 1996; Holsapple 2001, 2004). Zhang et al. (2017) investigated the plausible physical properties of Didymos A using soft-sphere discrete element method (SSDEM) simulations. They explored the critical states of spinning self-gravitating aggregates, and confirmed for certain internal configurations that geostatic stability can be reached by shifting the bulk density within the range constrained by the current reference model. For example, they point out the current shape can be maintained with a material friction angle $\sim$39° (supposed to be high for the asteroid regolith material) and no extra cohesion, if the internal structure is restricted to hexagonal closest packing or high polydispersity packing. And the critical bulk density in such cases would be $\sim$2.660 $\mathrm{g\,cc^{-1}}$, which is high compared to the reference value, but still in the margin of error.

The above two bulk densities are taken as representative of two stages of the binary system evolution: $\sigma = 2.146\ \mathrm{g\,cc^{-1}}$ (hereafter denoted as 'observed') giving the case when the primary is spun-up

Table 1. Directly measured physical dynamical parameters of 65803 Didymos by Richardson et al. (2016).

Parameter	Symbol	Value
Secondary orbital period	T	11.920 h +0.004/−0.006 h
Distance between the centre of primary and secondary	L	1.18 km +0.04/−0.02 km
Rotation period of the primary	P	2.2600 h ±0.0001 h
Diameter ratio of the secondary to the primary	η	0.21 ± 0.03

to the critical spin limit, and $\sigma^{c} = 2.660\ \mathrm{g\,cc^{-1}}$ (hereafter denoted as 'calibrated') indicating the case that the primary is experiencing a YORP acceleration, but has not reached the spin limit. By using the radar shape model, we study and compare the surface stability of the primary under two controlled parameter groups; one is based on the observed values, and the other is determined by the calibrated bulk density. Note that the calibrated bulk density σ^{c} leads to a fictitiously large total mass of the primary, which does not agree with the direct measurements of the mean separation L and secondary orbital period T; we thus shrink the original shape model a little to reconcile these parameters. The shrinking ratio is calculated to be 0.93; then all parameters, except the bulk density and the shape model scale, can be held constant. For Didymos B, since our knowledge of its mass, size, and shape are very limited, we adopt the assumption that it has an overall triaxial-ellipsoid shape with axis ratios 1.56: 1.2: 1.0, with the long axis oriented to extend through Didymos A's centre and the short axis oriented perpendicular to the orbital plane (Michel et al. 2017; Yu et al. 2017).

The knowledge of the interior structures of Didymos' components is limited to date. Didymos A shows several typical features of rubble-pile asteroids, e.g. the oblate overall shape with obvious equatorial ridges, the low bulk density that may indicate relatively high porosity for an S-type asteroid (the solid density of S-type asteroid grains is estimated to be 3.1–3.8 g cc according to Britt et al. 2002), etc. This evidence leads us to the assumption that Didymos A may have a loose regolith layer on the surface, i.e. local small-scale avalanches may occur episodically at the unstable regions, which could be caused by various triggering processes, such as surface failure due to thermal fatigue, and ground shaking because of local structural creep (Quillen et al. 2016, 2018). In effect, these local-scale avalanches may lead to a slight surface mass redistribution, or to mass shedding with much more complex influence on the dynamics of the binary system. Before the spin state of the primary is accelerated to the critical limit that causes global distortion, these regional events may be the main force that shaped the binary's configuration today. A detailed look into these events will help define the implicit constraints of the observations on the dynamic evolution of the Didymos system.

2.2 Twisted surface debris flow on the local slope

The local slope would tend to be flattened out if there is no cohesion and friction forces. The stability condition of a slope depends on the geometric and physical properties of the material, as well as on the external perturbations that might trigger a landslide and cause local surface failure. For Didymos A, as mentioned above, the external perturbation could be from a local structural failure due to thermal fatigue fragmentation (Murdoch et al. 2014), or seismic shaking because of the internal structural creep (Cheng 2002), or the tidal load cycles due to the gravity of Didymos B (Harris et al. 2009). In a similar analysis, Yu et al. (2014) formulated the external forces felt by a local sandpile that sits on the surface of an asteroid going through a planetary encounter. The forces acting on a local debris flow on the surface of Didymos A will hold the same basic components: the gravity from the primary, the tidal force from the secondary, the supportive and resistive forces from the ground bed and surrounding materials, the centrifugal force due to the rotation of the primary, the convected inertia force due to the angular acceleration of the primary, and the Coriolis effect when the landslide is occurring.

In this section, we developed a SSDEM model to mimic the possible landslides and assess their risks of shedding off. As shown in Fig. 1, a small piece of granular layer is sampled to represent the local behaviour of the regolith material on Didymos A. For a given set of coordinates of any position at the surface, the normal vector of the local tangential plane is obtained using an explicit expression that represents the shape in analytic form (here we employed the spherical harmonics; see Section 2.3 for details). Then combining the gravitational field model and the rotation state of the primary, we can derive the local slope direction, which is the steepest descent direction of the effective potential along the tangential plane:

$$\boldsymbol{l} = -\nabla V_{s} + (\nabla V_{s} \cdot \hat{\boldsymbol{n}})\hat{\boldsymbol{n}}. \tag{1}$$

In equation (1), V_{s} describes the equivalent potential on the surface, which is composed of two parts, the centrifugal potential due to the autorotation, and the gravitational potential from the primary. $\hat{\boldsymbol{n}}$ indicates the unit normal vector of the surface (outwards). Noting that for the Didymos system, the tidal force from the secondary is always lower by 3–4 mag than the gravity from the primary, and that the convected inertia force is negligible (the primary is generally rotating around a fixed axis), the governing equation of the sliding motion is then formulated approximately as

$$m\boldsymbol{a}_{r} = -\nabla V_{s} + \boldsymbol{f}_{c} - 2m\boldsymbol{\omega} \times \boldsymbol{v}_{r}, \tag{2}$$

in which m is the mass of the regolith, $\boldsymbol{a}_{r}$ is the acceleration of the mass centre of the debris flow, $\boldsymbol{f}_{c}$ indicates the resultant contact force from the circumstance (the ground bed and surrounding regolith), $\boldsymbol{\omega}$ indicates the angular velocity vector of the primary, and $\boldsymbol{v}_{r}$ indicates the relative velocity with respect to the surface.

Equation (2) determines the behaviour of a sliding debris flow, i.e. the motion of the sampled regolith is driven primarily by the difference in geopotential of the surface, resisted by the contact forces from the circumstance, and twisted by the Coriolis effect. We focus on the landslides that have the risk of shedding off within a relatively short sliding distance (hereafter called unstable local debris flow, or LDF). Regarding the dimension of Didymos A, we define the supremum length of an unstable LDF to be below 10 m, i.e. the involved debris reaches the shedding speed within a sliding distance smaller than 10 m. The choice satisfies the local gravity and local tangential plane because both stay nearly invariant within such a short distance. By projecting equation (2) on to the local tangential plane, we find the trajectory of the sampled regolith depends mainly on two parameters: the tangential component of local gravity g_{t} (including the gravitational attraction and the centrifugal force), and the normal component of the angular velocity ω_{n}; both can be viewed as constants for a local landslide. We performed SSDEM

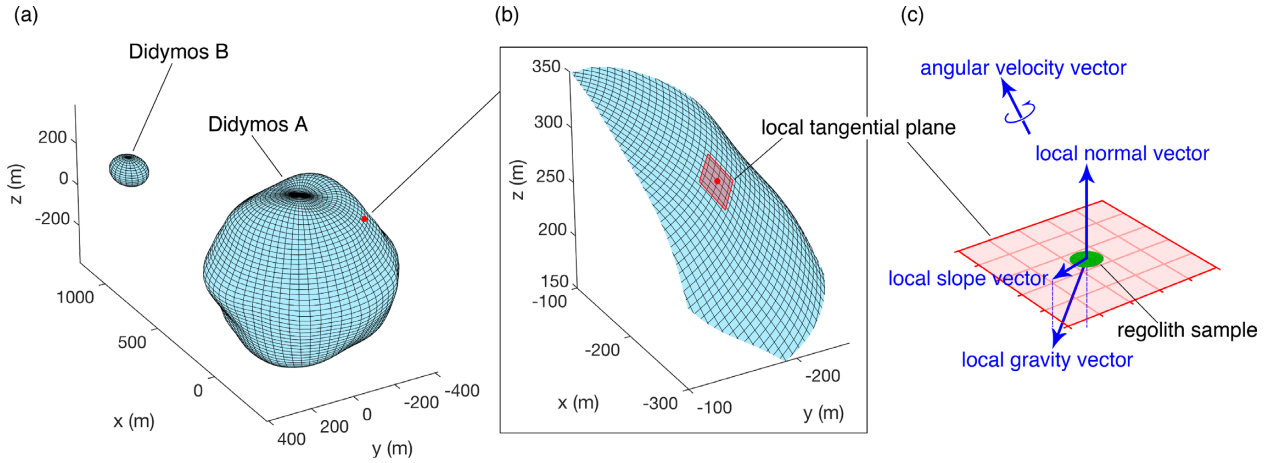

Figure 1. Diagram illustrating the orientation of a local regolith sample on the surface of Didymos A, serving as a gauge to the stability of the slope. The initial binary configuration and shape models of the binary components (a) are determined by following the observational results in Section 2.1. The zoom-in view (b) shows a local patch of the surface of Didymos A where the sampled regolith material is located. The tangential plane of Didymos A's surface at the location of the sampled regolith (b,c) is obtained in an explicit analytic shape model. Then in combination with the gravitational field model, the normal vector of the tangential plane determines the local slope direction in which a landslide (if it happens) will start to move.

simulations to capture the sliding speed and direction as functions of g_t and ω_n, using an extension of the parallel gravitational N-body package PKDGRAV (Richardson et al. 2005; Schwartz et al. 2012). As shown in Fig. 1(c) and Fig. 2(a), the regolith sample consists of $N = 6349$ spherical particles with radii drawn from a power-law distribution of mean 0.5 cm ±1 per cent (width truncated). The particles were initially laid out in a round shape of 54.0 cm diameter and to an even thickness of 4.5 cm, serving as a gauge to test the stability of a slope. Table 2 gives the basic physical properties of the simulated particles. It is notable we adopted the values suggested by Zhang et al. (2017) for the shear strength related parameters (k_t, β, μ_S, μ_T, μ_R), which are compatible with their analysis on Didymos' structural stability and give rise to a friction angle $\phi_r \approx 39^\circ$.

We calculated the allowed ranges of ω_n and g_t based on the reference model of Didymos (Section 2.1). A basic scope is obtained through a global search over the surface of Didymos A, which yields ω_n between -6.5×10^{-4} rad s^{-1} (South Hemisphere) and 6.5×10^{-4} rad s^{-1} (North Hemisphere), and g_t between 0.0 and 1.5×10^{-4} m s^{-2} according to the radar shape model. Fig. 2 shows an example of the local debris flow at $\omega_n = 3.25 \times 10^{-4}$ rad s^{-1}, $g_t = 9.50 \times 10^{-5}$ m s^{-2}. Snapshots of the sample particles at three simulated times are illustrated in Fig. 2(a), showing the twisting and diffusion of the involved regolith material on the local tangential plane. We notice at the initial stage of a local debris flow (<10 m), the average sliding speed v_r (the speed of the centre of mass) and the tilt angle θ (the angle of the sliding direction from the slope direction) both grow as linear functions of time. For example, in the case of Fig. 2, the slope fitting yields a rate of the tilt angle $\dot{\theta} \approx -1.16 \times 10^{-2\,\circ}$ s^{-1} (b) and a rate of the sliding speed $\dot{v}_r \approx 3.95 \times 10^{-5}$ m s^{-2} (c). We conducted a grid search over the parameter space spanned by $\omega_n \times g_t$, i.e. for each a pair of (ω_n, g_t) we ran a simulation to resolve the process of landslide. Noticing the symmetric form of equation (2), we considered the positive range of ω_n from 0.0 to 6.5×10^{-4} rad s^{-1} (the debris flow with $-\omega_n$ will be in mirror symmetry about the slope direction). The range of g_t in this experiment is from 0.4×10^{-4} to 1.5×10^{-4} m s^{-2}, which covers a wide range that allows a local landslide to be triggered.

Table 3 summarizes the results of the grid search. Each cell of the table shows the fit ratios of the tilt angle / sliding speed versus time for a given (ω_n, g_t). The ratios describe the statistic behaviour of the sampled particles at the initial stage of the landslide, i.e. the fits measure the twisting effect and acceleration of a surface debris flow down the slope direction, which are functions of the parameters ω_n and g_t. These functions are then approximated through a polynomial fit by equation (3).

$$\begin{aligned} \dot{\theta} &= \sum a_{ij} \omega_n^i g_t^j, \ 0 \le i, \ 0 \le j, \ i + j \le n, \\ \dot{v}_r &= \sum b_{ij} \omega_n^i g_t^j, \ 0 \le i, \ 0 \le j, \ i + j \le m. \end{aligned} \tag{3}$$

Table 4 presents the fitting results over the examined range, which are determined using a weighted linear least-square method. Degrees $n = 3$ and $m = 2$ for the polynomial were chosen to give an approximation with acceptable precision. Then equation (3) provides a semi-empirical expression that describes the behaviour of a local landslide occurring on the surface of Didymos A. In the following analyses, this formula will be applied to determine the sliding direction / speed at the early stage of a landslide, which helps to identify the unstable LDF that causes mass shedding over the entire surface of Didymos A.

2.3 Observation-based analysis of surface mass shedding

This section checks whether the reference model allows us to put new constraints on the surface stability of Didymos A. We consider loose regolith material that is released from the surface without any cohesive forces. The involved particles tend to start moving when the local slope angle ϕ exceeds the friction angle ϕ_r ($\phi_r \approx 39^\circ$ for our discussion). Equation (4) defines the slope angle in correlation with the local topography and local potential field:

$$\phi = \mathrm{acos}\left(\frac{-\nabla V_s \cdot \hat{\boldsymbol{n}}}{|\nabla V_s|} \right). \tag{4}$$

By definition, the partial surface corresponding to $\phi > \pi/2$ is an unstable region that cohesionless material cannot attach to or slide on; in contrast, the partial surface corresponding to $\phi < \phi_r$ is the stable region that allows the material to stick. We focus on the region with $\phi_r < \phi \le \pi/2$, for which the unstable LDF may probably lead

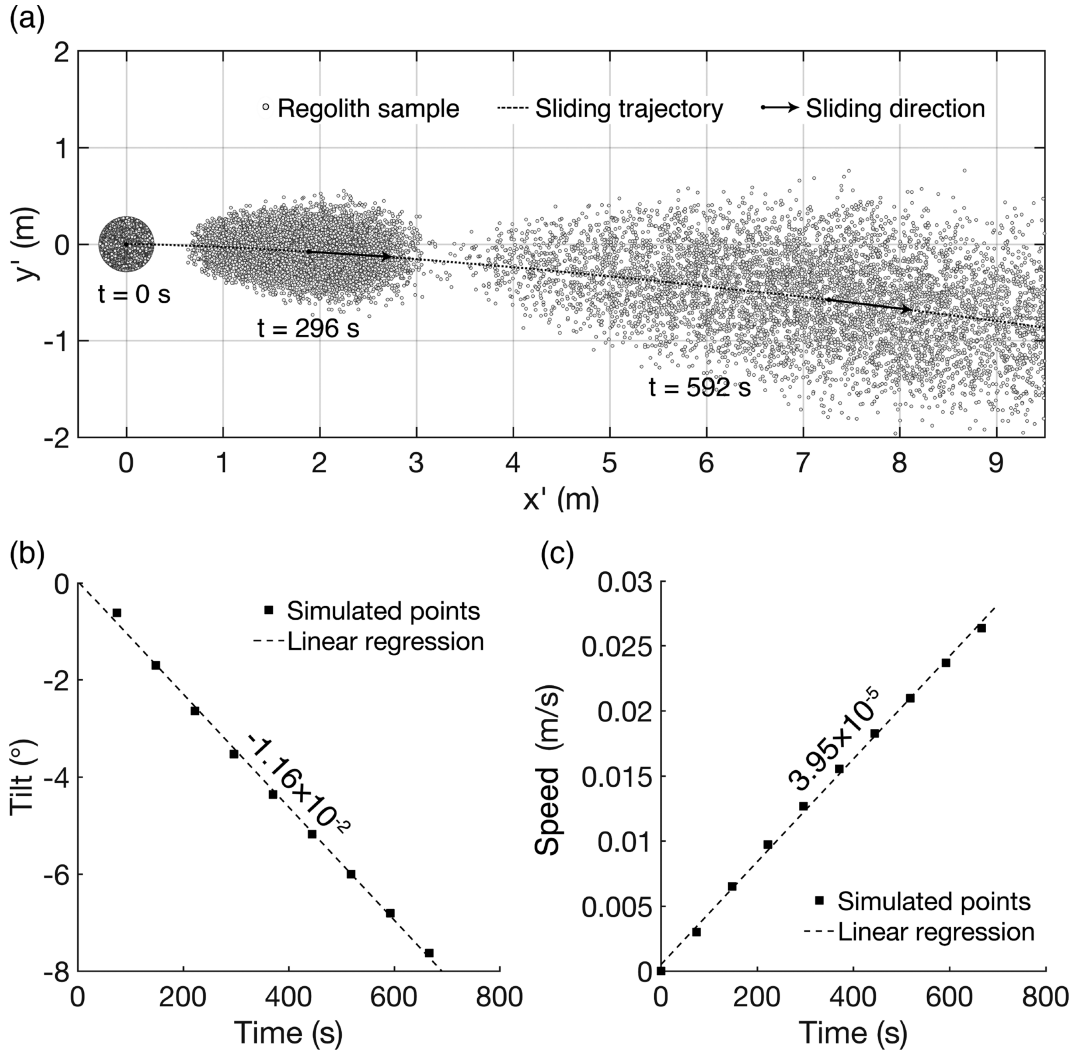

Figure 2. Detail of a local debris flow that extends ∼10 m at $\omega_n = 3.25 \times 10^{-4}$ rad s^{-1} and $g_t = 9.50 \times 10^{-5}$ m s^{-2}. Snapshots of the sample particles (a) are taken at three simulated times and then shown in a frame fixed to the local tangential plane (x'-axis points in the local slope direction, and right-handed z'-axis points along the local normal vector). The tilt angle θ (b) and the sliding speed v_r (c) of the debris flow are plotted versus time based on the averaged values at the simulated times (denoted by solid squares). The results of linear fits are shown by dashed lines, and the labelled numbers denote the slopes.

Table 2. Soft-sphere parameters used to represent the material properties of the regolith on the surface of Didymos A. Here the spring constants k_n, k_t are chosen according to the strategy presented by Schwartz et al. (2012), and the restitution coefficients ε_n, ε_t are chosen to match the damping features of ordinary rocks (Chau et al. 2002).

Parameter	Symbol	Value
Grain density	ρ_p	3400 kg m^{-3}
Normal spring constant	k_n	51.99 N m^{-1}
Tangential spring constant	k_t	14.85 N m^{-1}
Normal restitution constant	ε_n	0.55
Tangential restitution coefficient	ε_t	0.55
Shape parameter[a]	β	0.6
Static friction coefficient	μ_S	1.3
Twisting friction coefficient	μ_T	1.3
Rolling friction coefficient	μ_R	1.05

Note. [a]The shape parameter is defined to represent the statistical deviation of particle shape from spherical (Jiang, Shen & Wang 2015).

to a rapid mass shedding within a short distance (see Section 2.2). In a previous study, we represented the radar shape of Didymos A in spherical harmonics through a least-square fitting to the nodes of the polyhedron model (Yu et al. 2018), which could be formulated as

$$S(\lambda, \psi) = \sum_{l=0}^{\infty} \sum_{m=-l}^{l} c_l^m Y_l^m(\lambda, \psi), \tag{5}$$

in which c_l^m and $Y_l^m(\lambda, \psi)$ are the coefficients and bases of the harmonics, respectively (a detailed expression can be found in Yu et al. 2018). Equation (5) establishes an injective map from the spherical angles (λ, ψ) to the radial distance of the projected point on the surface, i.e. a parametric surface expression as a function of the geographic coordinates. By introducing a unit radial vector $\hat{\boldsymbol{r}}$, the surface expression in vector form yields $\boldsymbol{S} = S\hat{\boldsymbol{r}}$. It allows us to analyse theoretically the shedding-off condition of a landslide that happens at an arbitrary position on the surface. Particles involved in a landslide can be accelerated to critical speeds during the sliding process, which causes instantaneous separation of these particles

Table 3. Simulation results of grid searching over the parameter space $\omega_n \times g_t$. For each grid node (ω_n, g_t), the rate of the tilt angle $\dot{\theta}$ and the rate of the sliding speed $\dot{v}_r$ are obtained through linear fitting to the simulation data at the initial stage of the local landslide. Units: ω_n is given in 10^{-4} rad s^{-1}, g_t in 10^{-4} m s^{-2}, $\dot{\theta}$ in 10^{-2} $\circ$ s^{-1}, and $\dot{v}_r$ in 10^{-5} m s^{-2}.

	$\omega_n = 0.000$		$\omega_n = 1.625$		$\omega_n = 3.250$		$\omega_n = 4.875$		$\omega_n = 6.500$	
	$\dot{\theta}$	$\dot{v}_r$	$\dot{\theta}$	$\dot{v}_r$	$\dot{\theta}$	$\dot{v}_r$	$\dot{\theta}$	$\dot{v}_r$	$\dot{\theta}$	$\dot{v}_r$
$g_t = 0.400$	− 0.002	0.106	− 0.121	0.108	− 0.271	0.113	− 0.418	0.127	− 0.586	0.144
$g_t = 0.675$	− 0.003	1.719	− 0.394	1.719	− 0.818	1.734	− 1.227	1.742	− 1.640	1.759
$g_t = 0.950$	− 0.009	3.884	− 0.562	3.895	− 1.164	3.952	− 1.693	3.897	− 2.235	3.847
$g_t = 1.225$	0.008	6.224	− 0.636	6.226	− 1.289	6.218	− 1.935	6.234	− 2.560	6.124
$g_t = 1.500$	0.006	8.736	− 0.700	8.744	− 1.402	8.746	− 2.093	8.751	− 2.792	8.763

Table 4. The fitting results for equation (3) over the specified range, i.e. $0.0 \leq \omega_n \leq 6.5 \times 10^{-4}$ rad s^{-1}, $0.4 \times 10^{-4} \leq g_t \leq 1.5 \times 10^{-4}$ m s^{-2}. A weighted linear least-square method is used to calculate the fit. The residual measures the maximum absolute error at the grid nodes by using this fit. The units are kept consistent with those in Table 3.

Target function	$(\omega_n, g_t) \rightarrow \dot{\theta}$	$(\omega_n, g_t) \rightarrow \dot{v}_r$
Polynomial degree	$n = 3$	$m = 2$
Maximum residual	$\lvert\Delta\dot{\theta}\rvert_{\max} = 3.944 \times 10^{-4}$	$\lvert\Delta\dot{v}_r\rvert_{\max} = 1.065 \times 10^{-6}$
Coefficients	$a_{00} = 4.842 \times 10^{-3}$	$b_{00} = -1.978 \times 10^{-5}$
	$a_{10} = 2.175 \times 10^{1}$	$b_{10} = 2.017 \times 10^{-2}$
	$a_{01} = -1.898 \times 10^{2}$	$b_{01} = 4.329 \times 10^{-1}$
	$a_{20} = -6.228 \times 10^{3}$	$b_{20} = -1.923 \times 10^{0}$
	$a_{11} = -8.499 \times 10^{5}$	$b_{11} = -8.131 \times 10^{0}$
	$a_{02} = 2.156 \times 10^{6}$	$b_{02} = 1.894 \times 10^{3}$
	$a_{30} = 3.574 \times 10^{6}$	
	$a_{21} = 3.126 \times 10^{7}$	
	$a_{12} = 2.790 \times 10^{9}$	
	$a_{03} = -7.390 \times 10^{9}$	

from the body of the asteroid. The condition of lifting off the surface is that the normal supportive force becomes zero, i.e.

$$\boldsymbol{f}_c \cdot \hat{\boldsymbol{n}} = 0. \tag{6}$$

Combining equations (2) and (5), the lifting-off condition can be expanded as

$$\nabla V_s \cdot \hat{\boldsymbol{n}} + 2\boldsymbol{\omega} \times \boldsymbol{v}_r \cdot \hat{\boldsymbol{n}} + b^T \{\mathrm{I}\}^{-1,T} \{\mathrm{II}\} \{\mathrm{I}\}^{-1} b = 0, \tag{7}$$

in which $\{\mathrm{I}\}$, $\{\mathrm{II}\}$ indicate the first and second fundamental forms of the parametric surface $\boldsymbol{S}(\lambda, \psi)$. Let the subscripts λ, ψ indicate the partial derivatives with respect to spherical angles. These forms are defined as

$$\{\mathrm{I}\} = \begin{bmatrix} \boldsymbol{S}_\lambda \cdot \boldsymbol{S}_\lambda & \boldsymbol{S}_\lambda \cdot \boldsymbol{S}_\psi \\ \boldsymbol{S}_\lambda \cdot \boldsymbol{S}_\psi & \boldsymbol{S}_\psi \cdot \boldsymbol{S}_\psi \end{bmatrix}, \tag{8}$$

$$\{\mathrm{II}\} = \begin{bmatrix} \boldsymbol{S}_{\lambda\lambda} \cdot \hat{\boldsymbol{n}} & \boldsymbol{S}_{\lambda\psi} \cdot \hat{\boldsymbol{n}} \\ \boldsymbol{S}_{\lambda\psi} \cdot \hat{\boldsymbol{n}} & \boldsymbol{S}_{\psi\psi} \cdot \hat{\boldsymbol{n}} \end{bmatrix}. \tag{9}$$

The 2×1 array b indicates the sliding speed represented in the local surface frame:

$$b = \left[\boldsymbol{S}_\lambda \cdot \boldsymbol{v}_r, \boldsymbol{S}_\psi \cdot \boldsymbol{v}_r\right]^T. \tag{10}$$

Equations (6)–(10) provide a complete process of measuring the stability of Didymos A's surface: for a chosen surface point (λ, ψ), the harmonic shape model determines the geometric features, and the gravity can be calculated by using the polyhedral method proposed by Werner & Scheeres (1997); the slope angle ϕ is first applied to screen out the unstable region ($\phi_r < \phi \leq \pi/2$); then the averaged motion of a local landslide at the given point is determined by using the semi-empirical formula derived in Section 2.2 based on SSDEM simulation; the resulting sliding speed $\boldsymbol{v}_r$ as a function of time is then substituted into the left-hand side of equation (7), yielding a single-valued function of time $L(t)$. For the last step, we use $L(t)$ as a discriminator of the unstable LDF: searching the unstable region, we can identify the partial surface at high risk of mass shedding.

Fig. 3 illustrates the searching results using the two reference models presented in Section 2.1, i.e. (a) for the case with all parameters matched to the radar observation, and (b) for the case with the shape dimension adjusted according to the constraints of internal structural stability. A distribution of slope angle across the surface of Didymos A, the contour lines at different slope angles, and the analysis results on the LDF are jointly presented in the maps. In principle, this indicates whether loose regolith material is allowed to deposit, or tend to migrate, or even cause dangerous landslides that end with shedding mass from Didymos A. Recall that we defined the scale of the unstable LDF to be below 10 m; we see the regions denoted by the red lattice are actually at high risk of shedding off mass, i.e. the regolith involved in such an LDF will tend to escape at the initial stage of sliding.

Fig. 3 reveals the explicit features of the two considered reference models. For the 'observed' model, the polar areas are mostly stable due to the gentle slope angles. The strip area near the equator is the most unstable region, where the autorotation yields a larger centrifugal force than the gravity, thus cohesionless material should be rapidly cleared in this region and unweathered subsurface should be exposed. The partial surface at risk of unstable LDF appears close to the strip area and stretches out to mid-latitude. A dependence on the local topography is noticed for these high-risk regions, namely that the unstable LDF seems to only exist on the flats and bulges rather than the depressed terrains, which is consistent with the prediction of equation (7). For the 'calibrated' model, we see it

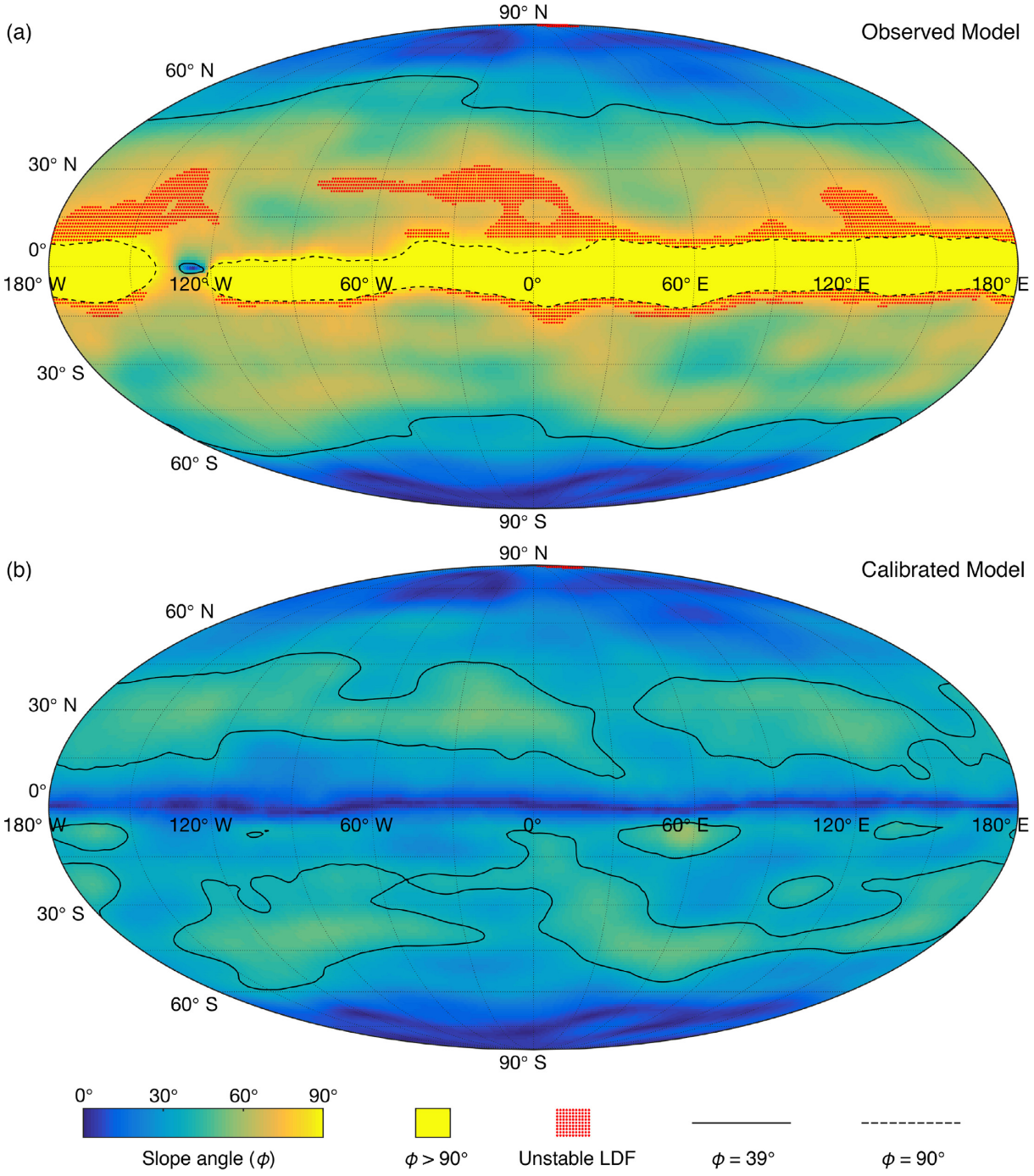

Figure 3. Geopotential slope mapped on the surface of Didymos A, in parallel with the analysis results on the stability of surface landslides. Two representative reference models are employed to generate the maps: (a) for the 'observed' model; (b) for the 'calibrated' model (see Section 2.1 for elaboration of the two models). The colour spectrum (blue–yellow) corresponds to slope angles (ϕ) ranging from 0° to 90°, and all areas satisfying $\phi > 90°$ are coloured in bright yellow. The solid and dashed curves indicate the contour lines of $\phi = 39°$ and $\phi = 90°$, respectively. The screening results of unstable LDF are marked in red lattices on the maps.

represents an evolution stage which is not very close to the critical spin limit, thus the polar and equatorial areas both have small slope angles, and areas of slope angles greater than the friction angle of regolith material ($\phi > \phi_r$) appear mainly in the mid-latitude. But no unstable LDF is observed across the wide mid-latitude regions, which means the overall risk of losing mass in this case is much smaller than that with the 'observed' model. However, a small strip area occupied by unstable LDF is noted at the North Pole in both cases, which corresponds to an oblique corridor shape near the North Pole.

3 DYNAMICS OF THE DEBRIS FLOW SHED FROM THE PRIMARY

This section focuses on the subsequent evolution of the shedding debris. Since the regional landslides are usually triggered by low-energy events, the relative speed of the regolith while separating from the surface is supposed to be small, i.e. not much extra energy is gained from the shedding process. Accordingly, once the shedding condition is instantaneously satisfied, the particles will enter a complicated phase of evolution, which is highly coupled with the interactions with the asteroid surface. These interactions are important factors that determine the ballistic motion of the shedding debris flow. We realize the fates of lofted particles exposed in such a complex environment are extremely diverse and exhibit strong dependence on the initial conditions and particle size. It is possible that a particle, after a stage highly coupled with the surface, gets stuck again and settles down on the surface (re-accretion), or gains enough energy so that it maintains a temporary low-altitude cycling orbit (with the periapsis close to the surface). The ultimate fates of the shedding debris could be escaping away from the binary system, causing cumulative mass-loss, or accreting on the binary components, causing a mass transfer.

3.1 Numerical simulations

Numerical experiments show that non-catastrophic reshaping occurs intermittently during YORP spin-up, but the disturbances from each reshaping only last for relatively short periods (Walsh et al. 2008). We assume no such violent distortion happens to the binary components during the surface mass shedding, which enables us to examine the surface process separately from the possible reshaping process. Considering a time span from several weeks to several months, the total mass-loss from the primary should be negligible compared to the mass of the asteroid. We apply a tracer model developed in previous studies to mimic the ballistic motion of particles shed from the unstable partial surface of the primary (Yu et al. 2017). In this model, we defined a closed system including the binary asteroid, the shedding particles and the Sun, i.e. four kinds of physical processes affecting the shedding particles were taken into account:

(1) Gravity from the primary;
(2) Gravity from the secondary;
(3) Tidal force due to the gravity from the Sun;
(4) Solar Radiation Pressure (SRP) acting on particles.

The primary (Didymos A) is considered as an irregular-shape polyhedron consisting of 1000 vertices and 1996 facets, and the secondary (Didymos B) is considered as a gravitational aggregate of solid spheres in the overall shape of a triaxial ellipsoid, so the gravitational effects in the vicinity of the two bodies can be assessed accurately (details are given in Yu et al. 2014); the gravitational influence of the shedding particles on the binary components are ignored. In each simulation, tracer particles are sampled randomly across the unstable regions on the primary (including both the $\phi > \pi/2$ region and the region occupied by the unstable LDF; see Fig. 3), then released with proper initial positions and velocities determined according to the analyses of Section 2.3. For the $\phi > \pi/2$ region, we assume the tracer particles lift off with zero relative velocities, and for particles from the unstable LDF, equations (3)–(10) give their velocities (directions and magnitudes) from the landslide when the shedding-off condition is met. Note that according to Section 2, the 'calibrated' model leads to a relatively stable surface that contains barely any unstable LDF, hence all the numerical results in this section are based on parameters of the 'observed' model.

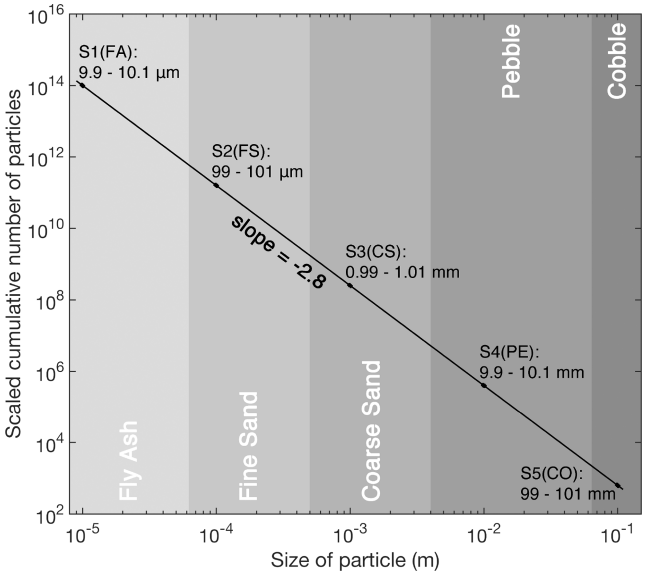

Figure 4. Strategy of sampling particles over the unstable partial surface. Five groups of sampled particles are chosen following the power-law size distribution and superimposed on the same log–log curve of a slope −2.8. The five groups of particles are denoted as S1–S5, and each represents a typical size range of the regolith grains (marked in bold white labels).

Fig. 4 summarizes the sampling strategy of particle sizes. Five groups of sample particles are considered as representative of regolith grains in different size ranges, i.e. group S1 for fly-ash grains (9.9–10.1 μm in diameter; abbrev. FA), S2 for fine-sand grains (99–101 μm in diameter; abbrev. FS), S3 for coarse-sand grains (0.99–1.01 mm in diameter; abbrev. CS), S4 for pebble grains (9.9–10.1 mm in diameter; abbrev. PE), and S5 for cobble grains (99–101 mm in diameter; abbrev. CO). We intentionally chose a concentrated size distribution for each of these groups (see Fig. 4), so we can get a clear-cut size dependence of the debris orbital motion. The cumulative size distribution of particles in these groups are generated following a power law of the same log–log slope −2.8, which is the reference value derived from the images taken by the HAYABUSA spacecraft of 25143 Itokawa (Miyamoto et al. 2007). It is an arbitrary choice to assume the full size range has a constant slope, because the slope −2.8 is measured based on relatively large particles (>0.1 m in size) on the surface of the asteroid. Nevertheless, we regard this hypothetical distribution as a gauge, which allows us to understand the size-sorting effect of the surface shedding process, and further, to estimate the long-term influence on regolith size distribution. The scaled cumulative number of particles is then defined as

$$\frac{N_{>d}}{N_{\rm r}} = d^{-2.8}, \tag{11}$$

where d is the diameter of a particle, $N_{>d}$ is the number of particles exceeding size d, and $N_{\rm r}$ is the reference number. According to equation (11), the fine-size particles have a larger number but a smaller mass ratio in the regolith sample (see Table 6 for the detailed mass proportions of different size ranges). We assign 138 195 tracer particles to each of the five groups, S1–S5. Such a large sample size is considered statistically meaningful to determine the particles' dynamical fates. As an S-type asteroid, the albedo of individual particles on Didymos A is assumed to be 0.15, based on the

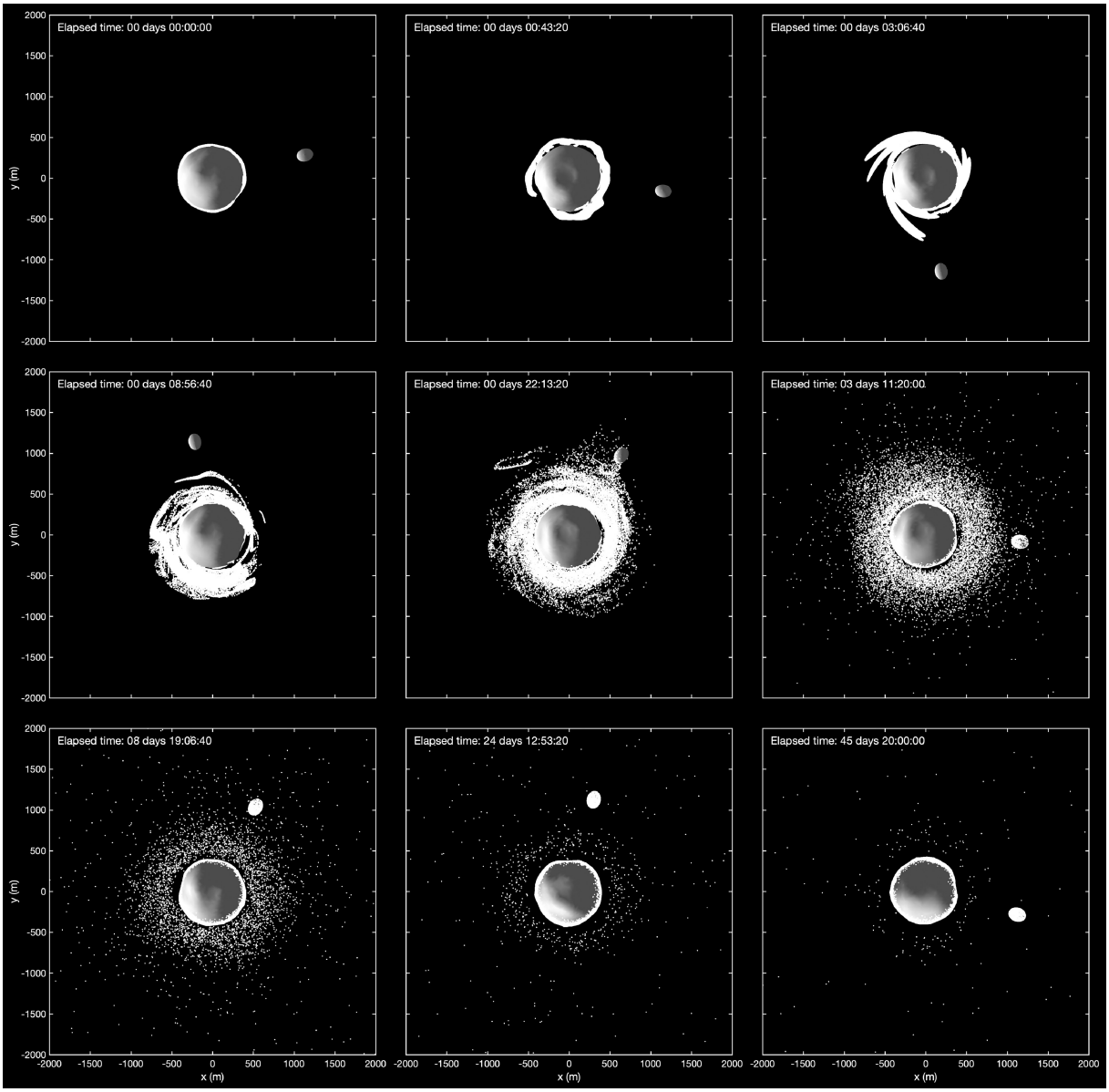

Figure 5. Snapshots of the time evolution of shedding particles in the control group S0 (view size ∼4 km). A fictitious large particle size is adopted for visual enhancement. (The reader is referred to the web version of this article for a complete movie of this evolution.).

meteorite analogue of ordinary chondrites. Simulations have been performed over 46.3 d of simulated time (4×10^6 sec), and a control group with zero albedo, denoted by S0, is provided to test the absolute influence of the SRP on particles of different sizes. The sample size of S0 remains the same as group S1–S5, i.e. 138 195 particles in total, and the size distribution is set to be the same as S4 (the pebble set), which is irrelevant since the solar radiation force has been turned off for the control group.

3.2 Results

Fig. 5 outlines the evolution of the shedding particles of the control group S0. The snapshots show representative configurations of the debris flow, which are selected for illustration over the simulation of ∼46 d. The snapshots demonstrate the complex dynamical behaviours of the shedding particles, which depend sensitively on the initial conditions. The non-spherical gravity of the primary and the gravity from the secondary exert periodic influences on the shedding particles, playing an important role in dispersing/accreting the debris cloud. However, there is still a small fraction of particles transferred into relatively sustainable orbits that survive to the end of the simulation. Group S0 serves as a benchmark for the post-shedding evolution. The simulation animations of S0 and the other five groups S1–S5 can be accessed in the supplemental materials (the evolution of the six groups are visualized in two parts: MOVIE22H.mp4 shows the first 22 h in slow motion while MOVIE46D.mp4 is a faster animation for the full 46 d).

Among the simulation results, four types of states of the shedding particles are considered at a given arbitrary time of the simulation: (1) On Surviving Orbit (OSO) – Until the given time limit, the particle has neither been intercepted by either of the binary components nor been ejected out of the binary system; (2) Re-accreting on the Primary (ROP) – Before the given time limit, the particle impacts and re-accretes on the surface of the Primary; (3) Accreting

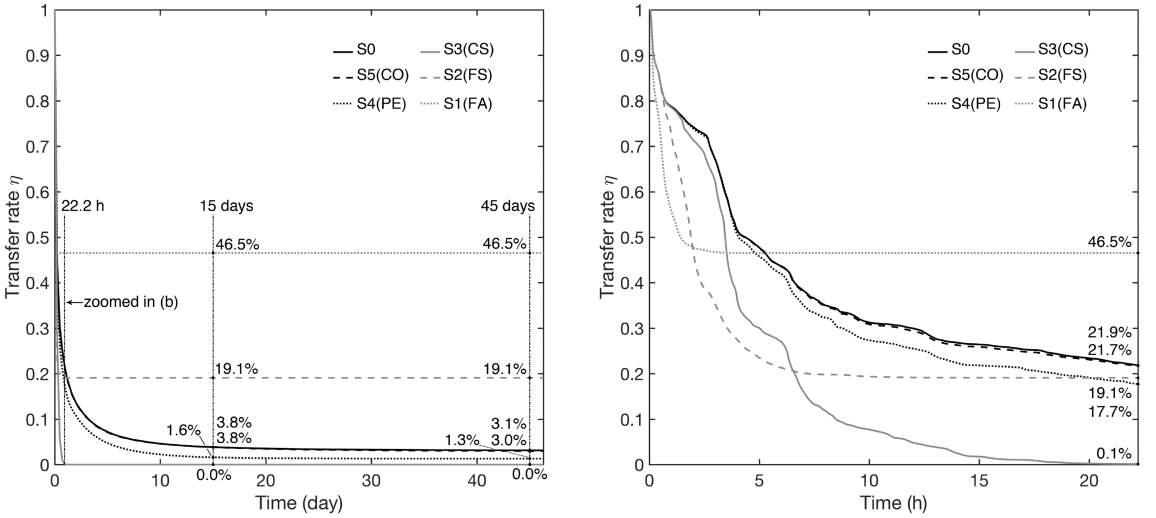

(a) Transfer rates over 46.3 days (b) Transfer rates in the first 22.2 h

Figure 6. Transfer rates (η) of the six simulated groups S0–S5, as functions of time. The six groups are indicated by six types of curves, i.e. dark solid, dark dashed, dark dotted, grey solid, grey dashed, and grey dotted, respectively (see the figure legend). The results of 46.3 d of simulated time are shown in panel (a), and a zoomed view of the first 22.2 h is shown in panel (b). Time labels and corresponding η values are included in the panels.

on the Secondary (AOS) – Before the given time limit, the particle impacts and accretes on the surface of the secondary; (4) Escaping out of the Sphere of Influence (ESI): Before the given time limit, the particle escapes away from the binary system, i.e. it is ejected out of the Sphere of Influence under the action of spin–orbit resonance. We assume that the particle sticks to its position at impact when it impacts either of the components (we call this 're-accretion' on the primary and 'accretion' on the secondary, considering the simulated particles originate from the primary). Note this assumption may not be true for particles colliding with Didymos A in our simulations, because we have shown that Didymos A may have a mostly unstable surface, and post-impact motion or bouncing can probably happen on this surface. In order to subtract the interference of these spurious results, in the following analysis, we intentionally removed the ROP particles from the set being analysed, i.e. at a given time, we define the effective set of the shedding particles to be the sum of the OSO particles, AOS particles and ESI particles, and use symbols $S0^t$–$S5^t$ to denote the effective sets of sample S0–S5 at time t, respectively. The effective set comprises the shedding mass that has been or is being transferred away from the primary. We also define the transfer rate for each simulated group as

$$\eta(t) = \frac{M_{S^t}}{M_S}, \tag{12}$$

in which M_{S^t} indicates the mass of the effective set at time t, and M_S indicates the total mass of its corresponding group.

Fig. 6 shows the transfer rates of the six simulated groups S0–S5 as functions of time. The effective sets of all six cases show a rapid decline in transfer rate, and achieve a steady rate within 15 d (Fig. 6a). A zoomed view of the first 22.2 h shows the initial decline rate (<1 h) is faster for smaller particle, and in particular, the fly-ash and fine-sand particles are transferred much faster than the other cases (Fig. 6b). In these two cases (FA & FS), the SRP exhibits a strong perturbation on the orbits of the shedding particles, so that the particles are rapidly blown off once they move out of the shadow region (defined as the region where the solar rays are blocked by Didymos A/B). Such a rapid cleanup effect leads to high transfer rates, which means fewer particles fall back to the primary's surface comparing to the cases with larger particle size. The curve of group S5(CO) almost coincides with that of the control group S0, showing that the motion of cobble particles is barely influenced by the SRP during their life cycles. As the particle size is reduced by ∼1 order of magnitude, as shown in the pebble case (PE), the transfer rate is reduced accordingly. We track the orbital motion of the shedding particles with/without SRP perturbation, and find that for pebble-size particles, the orbital changes resulting from SRP actually lead to more re-accretions on the primary's surface.

Table 5. An estimate of the relative strength of SRP versus surface gravity on Didymos A.

Group	SRP acc. ($m\,s^{-2}$)	Surf. grav. acc. ($m\,s^{-2}$)	Norm. SRP acc.
S0	–	2.36×10^{-4}	–
S1	2.30×10^{-4}	2.36×10^{-4}	9.76×10^{-1}
S2	2.30×10^{-5}	2.36×10^{-4}	9.76×10^{-2}
S3	2.30×10^{-6}	2.36×10^{-4}	9.76×10^{-3}
S4	2.30×10^{-7}	2.36×10^{-4}	9.76×10^{-4}
S5	2.30×10^{-8}	2.36×10^{-4}	9.76×10^{-5}

In Fig. 6, we find the post-shedding evolution at the early stage is extremely sensitive to the particle size. In order to estimate the relative strength of SRP, Table 5 lists the normalized SRP accelerations for all six groups, which are scaled using the surface gravity on Didymos A. In the cobble case, the surface gravity is $\sim 10^5$ times the magnitude of SRP; while in the fly-ash case, the surface gravity is identical in magnitude with SRP (the reader is referred to Yu et al. 2017 for a general discussion on the relative strength of SRP).

In our model, we define the final transfer rate η_f to be the value of $\eta(t)$ at the final time, which is defined as the time when the number of particles in the class OSO drops to zero, or when the default simulated time is reached. Then we compare the final transfer rates of groups S1–S5, and find it depends on the average particle size in a 'fall and rise' pattern: as the particle size increases, the final transfer rate decreases at first and then increases. Among the five groups, η_f reaches the minimum value at S3(CS), which represents

a typical case that demonstrates the diverse outcomes under SRP perturbation. For the coarse-sand particles, SRP acts as an efficient drag force to the cycling motion, i.e. once an OSO particle crosses the terminator line (from the shadow to the light), the head-on SRP significantly slows the speed down and degrades the orbital altitude, and thus the particle will impact the primary within a short time. In effect, this mechanism drives all the sampled particles of group S3 back to the surface of Didymos A in only 33.1 h (see Fig. 7d). This special case corresponds to zero final transfer rate, that finally all OSO particles become ROP, which suggests much fewer centimetre-sized regolith grains will be cleaned off the surface than other regolith constituents (larger or smaller in diameter).

It is notable that in this study we only counted the directly transferred particles. The definition of effective set excludes the ROP particles, which intentionally ignored all possible post-impact processes coming after the collisions. In reality, a re-accreting particle may bounce, hop, roll, twist, and slide on the surface and lift up again into cycling motion around the primary. Given the unstable surface of Didymos A, this possibility can be much higher than for the surface of a slowly rotating asteroid. An accurate assessment of the post-shedding evolution should consider the influence of these re-accreting particles by doing repeated iterations. However, our knowledge of the surface properties of Didymos A is very limited to date, which makes it difficult to calculate the impact outcomes of ROP particles. In the following discussion, we do analysis based on the normalized data of the effective sets, which we are aware could be slightly different from the true case. These results can be viewed as a benchmark for representing the statistics of the shedding particles' fates, which have a strong dependence on the average particle size.

The mass proportions of the effective sets of the six simulated groups S0–S5 are given in Fig. 7, shown as functions of time. Fig. 7(a) illustrates the results of the control group S0. The cobble case S5 (Fig. 7b) has almost identical mass proportions to S0, which confirms that SRP barely influences the post-shedding evolution of cobble particles. A considerable influence of the SRP perturbation is observed in the pebble case, S4 (Fig. 7c), which gives a higher percentage of AOS particles than the control group by ∼10 per cent at the end of simulated time. As the average particle size gets smaller, the influence of SRP becomes stronger. Fig. 7(d) shows the coarse-sand case, S3, for which particles are bounded closely to the primary's surface and no transferring to AOS/ESI occurs before the cycling particles totally vanish. We call the time when all OSO particles disappear from the simulated group to be the 'termination time'. This time shows a monotonic decrease as the particle size get smaller: the termination time is 33.06 h for group S3(CS), 30.56 h for group S2(FS), and 9.28 h for group S1(FA). Figs 7(e)–(f) show the cases in which the radiation pressure exerts dominant influences. In these cases, particles moving against the solar ray direction are de-accelerated rapidly, which creates a shower of debris on the light side of the primary; and particles moving in the opposite direction are accelerated rapidly, which creates an escaping flux along the direction of the solar ray. This process may last for a couple hours, and the particles initially moving in the shadows of the binary components may survive longer due to the solar occultation. The accretion of shedding mass on the secondary tends to be random in these cases, i.e. AOS particles can only exist if the secondary moves into the short-lived debris flux, which depends on the phase of the mutual orbit when mass shedding happens. Fig. 7(e) provides an example situation in which the debris showers on the surface of Didymos B; and Fig. 7(f) is for the situation in which no debris accretes on the surface of Didymos B.

The simulation results illustrated in Fig. 7 allow us to roughly estimate the total mass-loss/accretion of the shedding materials. We assume the power law matches a wide size range, i.e. equation (11) holds for the range 10 μm–10 cm, which is covered by groups S1–S5. This assumption is possibly true for the original regolith grains that were formed before the mass shedding, considered as a result of the natural weathering processes. The differential of equation (11) gives the density distribution of particle numbers:

$$\delta N = -2.8 N_{\rm r} d^{-3.8} \delta d; \tag{13}$$

then the mass distribution of particles of different sizes is determined by

$$\delta M = \frac{4\pi}{3} \rho_p \left(\frac{d}{2}\right)^3 \delta N. \tag{14}$$

Combining equations (13)–(14) and integrating with respect to the particle size d yields

$$M_{>d} = M_r - \frac{7\pi}{3} \rho_p N_{\rm r} d^{0.2}, \tag{15}$$

in which M_r is a reference value about the shedding mass. $M_{>d}$ indicates the total mass of the shedding regolith grains that exceed size d. To understand the mass distribution over the full size range, we choose a division of the specified range and calculate the shedding mass within each of the four subranges as listed in Table 6. The five nodes of the subranges, as shown, are taken at the sampled particle sizes of S1–S5, which therefore gives the subrange names as 'FA–FS', 'FS–CS', 'CS–PE', and 'PE–CO'. The mass that distributes in each subrange is scaled by the total mass of the full size range, so the sum of the four scaled values yields 1. For each subrange, we use the simulation results at 46.3 d to estimate the possible mass proportions of ESI and AOS particles. Because all five simulations are nearly completed at 46.3 d (see Fig. 7), these estimated proportions should reflect the final states of the shedding materials. Taking subrange FA–FS as an example, Figs 7(e)–(f) show at the end of the simulations that the mass percentages of ESI particles are 99.58 per cent and 100 per cent, respectively. Then given that FA–FS particles only count for 11.02 per cent of the total shedding mass, this determines an interval 10.97–11.02 per cent for the estimate of ESI particles from this subrange.

The estimates given in Table 6 reveal several features of the shedding regolith grains: (1) Bigger particles comprise more of the shedding mass, and the mass percentage grows slowly with the average particle size; (2) The majority of the shedding mass (calculated based on the effective set) fall into the AOS type, i.e. accrete on the secondary and build-up a bigger moonlet; (3) Almost all of these new blocks of the secondary come from particles greater than 1 mm in diameter (above coarse sand), and the contribution from dust-size particles (<1 mm) is negligible; (4) The escaping flux of shedding materials comprises the vast majority of particles below 1 mm, and a small fraction of the pebble–cobble particles.

Based on the results in Table 6, we further estimate the angular momentum delivered to the secondary. Since the total shedding mass we considered in this study is still too small to cause any perceptible orbital shift of Didymos B, we define a transfer coefficient χ that describes the relative deviation of angular momentum carried by a unit mass.

$$\chi = \frac{(\mathrm{d}\boldsymbol{L}/\mathrm{d}m - \boldsymbol{L}_{\rm s}/m_{\rm s}) \cdot \hat{\boldsymbol{L}}_{\rm s}}{|\boldsymbol{L}_{\rm s}/m_{\rm s}|}, \tag{16}$$

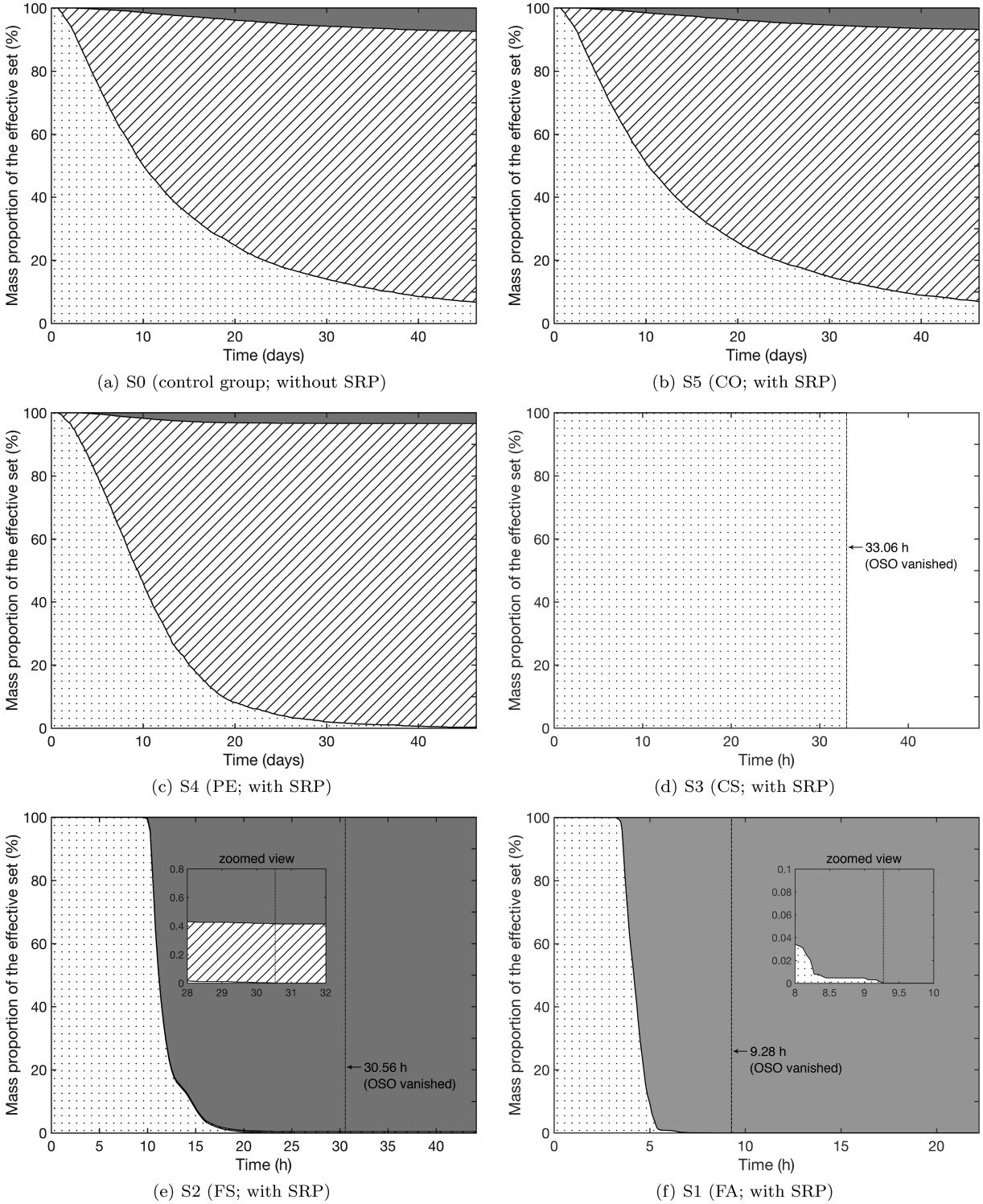

(a) S0 (control group; without SRP)
(b) S5 (CO; with SRP)
(c) S4 (PE; with SRP)
(d) S3 (CS; with SRP)
(e) S2 (FS; with SRP)
(f) S1 (FA; with SRP)

Figure 7. Mosaic of mass proportion evolution of the effective sets for the six simulated groups S0–S5, one panel per group. The dynamical fate proportions are indicated with shadowed areas. The solid shadow is for the proportion of ESI particles; the oblique shadow is for AOS particles; and the dotted shadow is for OSO particles. The dashed line and labelled arrow mark the termination time when all OSO particles are cleaned from the simulated group. Local zoomed views around the termination time are shown in panels (e)–(f).

in which dm indicates the accreting mass of a single AOS impact (an AOS impact is defined as the impact from an AOS particle), and d$\boldsymbol{L}$ indicates the angular momentum carried by the accreting mass; $m_{\rm s}$ and $\boldsymbol{L}_{\rm s}$ are the mass and angular momentum of the secondary, and $\hat{\boldsymbol{L}}_{\rm s}$ is the unit vector of $\boldsymbol{L}_{\rm s}$. At the moment when an AOS particle impacts the secondary, χ describes how the mutual orbit will change. A positive χ means that the impact accelerates the secondary slightly and tends to expand the mutual orbit, while a negative χ means that the impact decelerates the secondary slightly and tends to degrade the mutual orbit. As stated above, a vast

Table 6. Mass distribution over the full size range 10 μm–10 cm.

Subrange	Particle diameter	Mass (per cent)	Estimate ESI (per cent)	Estimate AOS (per cent)
FA–FS	10–100 μm	11.02	10.97–11.02	0–0.05
FS–CS	100 μm–1 mm	17.46	0–17.39	0–0.07
CS–PE	1 mm–1 cm	27.67	0–0.94	0–26.64
PE–CO	1 cm–10 cm	43.85	1.49–2.99	37.82–42.21

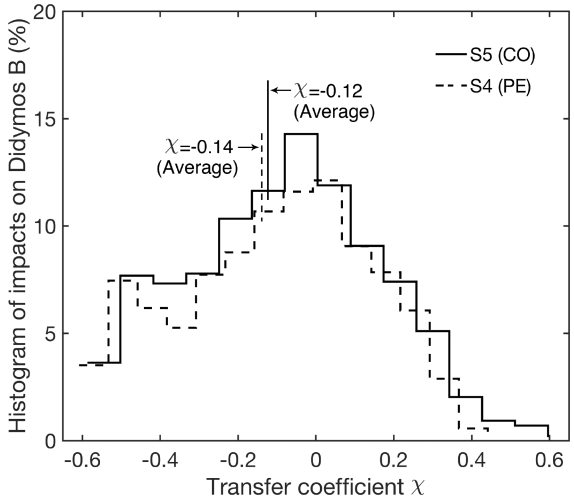

Figure 8. Histograms of the AOS impacts from group S4 (dashed line) and group S5 (solid line), calculated based on the simulation results at 46.3 d. The bin counts are given as percentages, and the averaged values of the transfer coefficient are marked using labelled arrows for both cases.

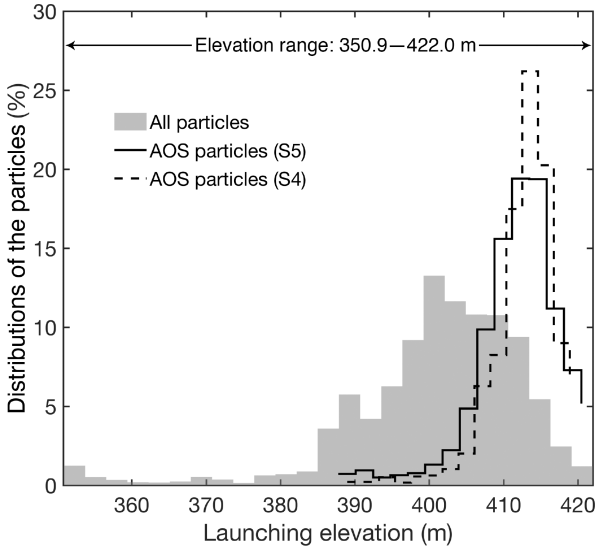

Figure 9. Distributions of the AOS particles in groups S4 (dashed lines) and S5 (solid lines) over their launching elevations, versus those of all the sampled particles (grey bins). The bin counts are given as percentages.

majority of the AOS impacts are from bigger particles (PE–CO), so we can infer that the angular momentum transfer is dominated by the same subrange. We calculated the transfer coefficients based on the simulation results of groups S4(PE) and S5(CO), and show the statistics of all AOS impacts in Fig. 8.

The histograms in Fig. 8 suggest that the overwhelming outcome of the AOS impacts will be to reduce the mean angular momentum $|\boldsymbol{L}_s/m_s|$ and cause Didymos B to spiral towards its primary, because a statistical analysis gives an average value $\bar{\chi} = -0.12$ for the cobble particles, and -0.14 for pebble particles. These are relatively large numbers according to equation (16), e.g. a 10 per cent increment in the secondary's mass will lead to a 3–4 per cent drop in the mutual orbit period. An estimate of the total effect of this 'shedding debris drag' depends on many variables that are barely known, like the frequency and volume of the surface mass shedding, and the size distribution of the shedding grains, etc. Therefore, we cannot determine how strong this effect is and what role it played in the geological history of the Didymos system. The mutual evolution of a binary system is complex and sensitive to many factors (Goldreich & Sari 2009; Ćuk & Nesvorný 2010; Jacobson & Scheeres 2011). Nevertheless, there are certain points to make: (1) The current reference model of the Didymos system dynamics allows intermittent mass shedding from the primary's surface; (2) The current phase of Didymos B has an advantage in accumulating the shedding mass; (3) The cumulation of shedding mass may cause immediate spiralling-in of Didymos B towards Didymos A, which is a more rapid mechanism than the mutual tides/BYORP, but it is uncertain how sensitively this drag effect depends on the binary dynamics. General discussion of the long-term effect of shedding debris drag should be part of a future study.

Finally, we look into the topography dependence of the AOS particles. Since simulations of S4 and S5 show the size of Didymos B is likely to grow by accumulating the bigger particles shed from Didymos A, we focus on a detailed process of such material exchange. In particular, we track back the AOS particles in S4 and S5, and map out the launching positions of these particles on the surface of Didymos A (see Fig. 3a; a description of the mapping technique can be found in Yu et al. 2018). We find in both cases, the launching positions of AOS particles exhibit a distribution highly weighted to the high-elevation regions (Fig. 9). Histograms in Fig. 9 show the launching elevations of the AOS particles versus the launching elevations of all the sampled particles. The full range of launching elevations of all sampled particles in S4/S5 is 350.9–422.0 m, as indicated in the figure. The average launching elevation of AOS particles is 411.9 m for S4 (pebble particles), and 410.9 m for S5 (cobble particles). On average, the distribution of AOS particles shifts greatly towards the high-elevation side, compared with the original distribution of all particles.

More specifically, we find the AOS particles mostly distribute in the bulged areas of the equatorial ridge, e.g. around (90°W, 0°S/N), (40°E, 0°S/N), and (170°E, 0°S/N). These bulges are also occupied by areas of elevation greater than 400 m. Dynamically this means particles shed from these areas have better chances to survive from collisions with the primary and to be transferred straight to the secondary. It makes a direct transfer channel that enables efficient mass exchange between the two components. Consequently, this

might provide a secular mechanism to erode the bulges of the equatorial ridge and to force the primary's equator to evolve into good roundness, which could work until the spin rate exceeds the catastrophic limit that causes global disruption (Tardivel, Sánchez & Scheeres 2017).

4 CONCLUSION

In this paper, we study the plausible mass shedding from the surface of the primary of 65803 Didymos, and the subsequent orbital expansion of the shedding debris. The influences of sophisticated surface topography and non-spherical gravitational field are both considered, and the results reveal that these asymmetries play a significant role in the initial shedding processes as well as in the subsequent orbital evolution.

For the first part of the paper, we derive the conditions of surface mass shedding, which are applied to the reference model of Didymos A (the primary). An observation-based estimate of the surface stability is obtained, which combines the results of SSDEM simulations and a semi-analytical analysis of surface avalanches. From this estimate, we find that the 'observed' reference model suggests a highly unstable surface. A strip area is revealed near the equator in which the centrifugal force is larger than the gravity, so any cohesionless material will be shed off immediately. Along this strip area, there is an irregular high-risk region that stretches out from the equator to mid-latitude. In this region, the slope angle exceeds the estimated friction angle, and materials involved in a local debris flow will be accelerated to separation speed in a very short sliding distance. Thus landslides of loose regolith materials that cause mass shedding are likely to happen in this region, and unweathered materials should be exposed in a vast area around the equator. A dependence on the local topography is also noticed, such that the landslide-induced mass shedding seems to favour the flats and bulges, rather than the depressed terrains. We believe such a weathering process has an effect of flattening out the equatorial bulges. We also checked a 'calibrated' reference model of Didymos A that has a larger bulk density. The results show it has a relatively stable surface, i.e. the centrifugal force is always smaller than the gravity normal component, so no detachable area is found. Local slopes steeper than the friction angle are observed at mid-latitude, but differ from the high-risk region stated above; landslides in this area are unlikely to cause extensive mass shedding.

For the second part, we track the orbital motion of shedding particles sampled over the unstable region defined in the first part, and show statistics of their dynamical fates based on the simulation results. We find a strong size-sorting effect in the orbital expansion of the shedding debris. Sample particles sized from fly ash to cobble exhibit diverse evolutions, due to the varying magnitude of SRP acceleration. The cobble-size particles are barely influenced by SRP during the whole life cycle, and a high percentage of the shedding particles finally accrete on Didymos B. The influence of SRP grows as particle size decreases. For fly-ash particles, SRP becomes dominant and can rapidly blow off all particles outside the shadow region. It is noticed a certain magnitude of SRP (e.g. for coarse-sand particles in our simulations) is capable of driving all the shedding particles of similar sizes back to the surface of the primary, which may cause a long-term impact on the size distribution of regolith grains on Didymos A. Statistics of the mass proportion shows that the majority of the shedding mass is finally transferred to Didymos B, and almost all the added mass comes from bigger particles (pebble–cobble size). The added mass to the secondary, according to our calculation, carries a lower mean angular momentum than the secondary itself. This means cumulative mass transfer may produce a drag force that causes the secondary to spiral in towards the primary. This is a more rapid mechanism than the mutual tides/BYORP that determine the binary's configuration. A future work should be organized to find how this 'shedding debris drag' depends on the current binary dynamics. We also track back the source area of the added mass to Didymos B, and find it mostly distributes in the high-elevation region of Didymos A, i.e. the bulges of the equatorial ridge. This confirms the flattening effect as mentioned above, namely that the shedding processes prefer to erode the bulges first and force the equatorial ridge to evolve into good roundness.

The ongoing AIDA mission project may provide a unique opportunity to understand the physics explored in this study. Science returns of the mission will shed light on mysteries like how the low-speed ejecta cloud (comprised in the slow ejecta curtain) will survive in the binary system, and how the debris interplay with the binary components. It will improve greatly our knowledge of the mass-shedding processes on a fast-rotating, top-shaped asteroid, and will guide our future studies on the growth limit of the moonlet.

ACKNOWLEDGEMENTS

YY acknowledges support from the Natural Science Foundation of China (Grants No. 11702009 & No. 11525208). The simulations were performed using the cluster Tianhe-2 located in the Chinese National Supercomputer Center.

REFERENCES

Benner L. A. M., Margot J., Nolan M. C., Giorgini J. D., Brozovic M., Scheeres D. J., Magri C., Ostro S. J., 2010a, Bulletin of the American Astronomical Society, 42, 1056

Benner L. A. M., Margot J., Nolan M. C., Giorgini J. D., Brozovic M., Scheeres D. J., Magri C., Ostro S. J., 2010b, American Astronomical Society Division for Planetary Sciences Meeting, Radar Imaging and a Physical Model of Binary Asteroid 65803 Didymos. Pasadena, California, 13.17

Benner L. A. M., Busch M. W., Giorgini J. D., Taylor P. A., Margot J. L., 2015, in Michel P., DeMeo F. E. et al., eds, Asteroids IV. University of Arizona Press, Tucson, p. 165

Bottke W. F., Cellino A., Paolicchi P., Binzel R. P., eds, 2002, Asteroids III. University of Arizona Press, Tucson, p. 395

Britt D. T., Yeomans D., Housen K., Consolmagno G., 2002, in Bottke W. F., Cellino A., Paolicchi P., Binzel R. P., eds, Asteroids III. University of Arizona Press, Tucson, p. 485

Brozović M. et al., 2011, Icarus, 216, 241

Busch M. W. et al., 2011, Icarus, 212, 649

Chau K. T., Cheng M., Chan C. C., 2002, Int. J. Rock Mech. Min. Sci., 38, 2382

Cheng A. F., 2002, in Warmbein B., ed., ESA SP-500: Seismic Shaking: Implications for Surface and Interior Structure of 433 Eros. ESA, Noordwijk, p. 733

Cheng A. F. et al., 2016, Planet. Space Sci., 121, 27

Clark B. E., Hapke B., Pieters C., Britt D., 2002, in Bottke W. F., Cellino A., Paolicchi P., Binzel R. P., eds, Asteroids III. University of Arizona Press, Tucson, p. 585

Cotto-Figueroa D., Statler T. S., Richardson D. C., Tanga P., 2015, ApJ, 803, 25

Ćuk M., 2007, ApJ, 659, L57

Ćuk M., Nesvorný D., 2010, Icarus, 207, 732

Dell'Elce L., Baresi N., Naidu S. P., Benner L. A. M., Scheeres D. J., 2017, Adv. Space Res., 59, 1304

Goldreich P., Sari R., 2009, ApJ, 691, 54

Harris A. W., 1996, Lunar Planet. Sci., 27, 493

Harris A. W., Fahnestock E. G., Pravec P., 2009, Icarus, 199, 310
Hirabayashi M., Sánchez D. P., Scheeres D. J., 2015, ApJ, 808, 63
Hirabayashi M. et al., 2016, Nature, 534, 352
Holsapple K. A., 2001, Icarus, 154, 432
Holsapple K. A., 2004, Icarus, 172, 272
Jacobson S. A., Scheeres D. J., 2011, ApJ, 736, L19
Jiang M., Shen Z., Wang J., 2015, Comput. Geotech., 65, 147
Kaasalainen M., Ďurech J., Warner B. D., Krugly Y. N., Gaftonyuk N. M., 2007, Nature, 446, 420
Michel P. et al., 2018, Adv. Space Res., 62, 2261
Miyamoto H. et al., 2007, Science, 316, 1011
Murdoch N., Penttilä A., Granvik M. , Virkki A., Fedorets G., Wilkman O., Kohout T. , 2014, in Muinonen K. , et al. Proc. Asteroids, Comets, Meteors 2014. Helsinki, Finland, p. 399
Nolan M. C. et al., 2013, Icarus, 226, 629
Ostro S. J. et al., 2006, Science, 314, 1276
Pravec P. et al., 2006, Icarus, 181, 63
Pravec P. et al., 2010, Nature, 466, 1085
Pravec P., Harris A. W., Kušnirák P., Galád A., Hornoch K., 2012, Icarus, 221, 365
Quillen A. C., Giannella D., Shaw J. G., Ebinger C., 2016, Icarus, 275, 267
Quillen A. C., Zhao Y., Chen Y., Sánchez P., Nelson R. C., Schwartz S. R., 2018, Icarus, 319, 312
Richardson D. C., Elankumaran P., Sanderson R. E., 2005, Icarus, 173, 349
Richardson D. C. et al., 2016, 47th Lunar and Planetary Science Conference. Woodlands, Texas, United States, p. 1501
Rubincam D. P., 2000, Icarus, 148, 2
Scheeres D. J., 2007, Icarus, 189, 370
Scheeres D. J., 2015, Icarus, 247, 1
Scheirich P., Pravec P., 2009, Icarus, 200, 531
Schwartz S. R., Richardson D. C., Michel P., 2012, Granular Matter, 14, 363
Statler T. S., 2009, Icarus, 202, 502
Tardivel S., Sánchez P., Scheeres D. J., 2018, Icarus, 304, 192
Taylor P. A. et al., 2007, Science, 316, 274
Walsh K. J., Jacobson S. A., 2015, in Michel P., , Bottke W. F. et al., eds, Asteroids IV. University of Arizona Press, Tucson, p. 375
Walsh K. J., Richardson D. C., Michel P., 2008, Nature, 454, 188
Walsh K. J., Richardson D. C., Michel P., 2012, Icarus, 220, 514
Werner R. A., Scheeres D. J., 1997, Celest. Mech. Dyn. Astron., 65, 313
Yu Y., Richardson D. C., Michel P., Schwartz S. R., Ballouz R.-L. , 2014, Icarus, 242, 82
Yu Y., Michel P., Schwartz S. R., Naidu S. P., Benner L. A. M., 2017, Icarus, 282, 313
Yu Y., Michel P., Hirabayashi M., Schwartz S. R., Zhang Y., Richardson D. C., Liu X., 2018, AJ, 156, 59
Zhang Y. et al., 2017, Icarus, 294, 98

SUPPORTING INFORMATION

Supplementary data are available at *MNRAS* online.

MOVIE46D.mp4
MOVIE22H.mp4

Please note: Oxford University Press is not responsible for the content or functionality of any supporting materials supplied by the authors. Any queries (other than missing material) should be directed to the corresponding author for the article.

This paper has been typeset from a TEX/LATEX file prepared by the author.